

## Size Matters: Another Reason Why the Atlantic Is Saltier than the Pacific

C. S. JONES AND PAOLA CESSI

*Scripps Institution of Oceanography, University of California, San Diego, La Jolla, California*

(Manuscript received 7 April 2017, in final form 21 September 2017)

### ABSTRACT

The surface salinity in the North Atlantic controls the position of the sinking branch of the meridional overturning circulation (MOC); the North Atlantic has higher salinity, so deep-water formation occurs there rather than in the North Pacific. Here, it is shown that in a 3D primitive equation model of two basins of different widths connected by a reentrant channel, there is a preference for sinking in the narrow basin even under zonally uniform surface forcing. This preference is linked to the details of the velocity and salinity fields in the “sinking” basin. The southward western boundary current associated with the wind-driven subpolar gyre has higher velocity in the wide basin than in the narrow basin. It overwhelms the northward western boundary current associated with the MOC for wide-basin sinking, so freshwater is brought from the far north of the domain southward and forms a pool on the western boundary in the wide basin. The fresh pool suppresses local convection and spreads eastward, leading to low salinities in the north of the wide basin for wide-basin sinking. This pool of freshwater is much less prominent in the narrow basin for narrow-basin sinking, where the northward MOC western boundary current overcomes the southward western boundary current associated with the wind-driven subpolar gyre, bringing salty water from lower latitudes northward and enabling deep-water mass formation.

### 1. Introduction

In the current climate system, deep water is formed in the North Atlantic but not in the North Pacific, resulting in a meridional overturning circulation (MOC) that transports heat northward everywhere in the Atlantic. Deep-water formation in the North Pacific is prevented by fresh, buoyant surface waters, much fresher than surface waters at comparable latitudes in the Atlantic (Warren 1983; Broecker 1991), with the salinity component dominating over the temperature component (the colder and fresher North Pacific surface water is lighter than the warmer and saltier North Atlantic surface water). Several reasons have been advanced for the salinity difference between the Atlantic and the Pacific [see Weaver et al. (1999) for a review].

The flux of freshwater into the atmosphere from the ocean may be expressed as the evaporation minus precipitation ( $E - P$ ) rate per unit area. Craig et al. (2016) show that  $E - P$ , integrated over each basin north of 35°S, is greater in the Atlantic than in the Pacific by 0.4 Sv (1 Sv ≡  $10^6 \text{ m}^3 \text{s}^{-1}$ ); the net  $E - P$  out of the Atlantic is about 0.4 Sv and approximately zero out of the

Pacific. Several mechanisms contribute to the difference in  $E - P$  between oceans, some involving the atmosphere alone and others involving the ocean circulation. The North Pacific experiences slightly higher precipitation because of the more effective orographic blockage of moist air in the Pacific sector (Broecker et al. 1990; Schmittner et al. 2011). However, Kamphuis et al. (2011) show that Atlantic sinking still occurs on a retrograde-rotating Earth, where the direction of the winds across the American continent are reversed. This implies that the orographic blockage of moisture transport by the American continent alone does not set the location of deep-water formation. The northward transport of moisture by the Asian monsoon (Geay et al. 2003) in the Pacific sector may contribute to the higher precipitation in the north of that basin, suppressing local sinking. The precipitation footprint of water evaporating from the narrow Atlantic basin extends into the wider Pacific basin, while most of the water evaporating from the Pacific precipitates in the same sector (Ferreira et al. 2010; Wills and Schneider 2015). In addition, a larger fraction of the area of the Atlantic is exposed to dry air coming off the continents, which may also increase evaporation over the Atlantic (Schmitt et al. 1989).

Corresponding author: C. S. Jones, csjones@ucsd.edu

Some of the geographical differences between the two ocean basins are thought to favor deep-water formation in the North Atlantic. Most obviously, the Atlantic extends farther north than the Pacific, and it is more connected to the Arctic, where cold dense water is formed during winter (Warren 1983). Mixing with the outflow from the Mediterranean Sea (a semienclosed basin with net evaporation) may increase the salinity of the northward branch of the MOC (Reid 1979; Warren 1981), although the importance of this process has been questioned (McCartney and Mauritzen 2001; Talley 2008). The larger width of the Pacific, and associated stronger wind-driven circulation and east–west temperature contrasts, may produce a larger poleward heat transport by the gyres in the Pacific relative to the Atlantic, removing the need for a MOC-mediated heat transport (Wang et al. 1995). The lower-latitude position of the tip of South Africa relative to the tip of South America is a favorable configuration for transporting high-salinity water from the Indo-Pacific sector into the Atlantic (Reid 1961; Gordon et al. 1987; Cessi and Jones 2017). Finally, the surface branch of the MOC advects higher-salinity waters from the subtropics to the high latitudes, further enhancing the salinity in the North Atlantic relative to the North Pacific. This process is termed “the salt–advection feedback” (Stommel 1961).

At least some of the explanations for a saltier Atlantic rely on the Atlantic meridional overturning circulation (AMOC), which is itself enabled by increased salinity in the North Atlantic. Salt (and heat) advection feedbacks act to maintain the MOC and higher salinity (and temperature) in the region where the deep-water formation takes place. Higher temperatures decrease the surface density and thus tend to reduce the overturning rate, that is, a negative feedback. Higher salinities increase the surface density and thus directly increase the overturning rate, while higher temperature tends to decrease the overturning rate. In principle, the salt advection feedback could act to produce deep overturning in the Pacific [Pacific meridional overturning circulation (PMOC)] rather than in the Atlantic. However, both coupled (Ferreira et al. 2010; Nilsson et al. 2013) and ocean-only idealized models (Stocker et al. 1992; Hughes and Weaver 1994) show a preference for sinking in the narrower basin. Huisman et al. (2012) even find that Atlantic sinking occurs when  $E - P$  is higher in the Pacific than in the Atlantic, indicating that the oceanic transport of salt controls the location of sinking.

It is important to understand the reasons why the Atlantic is saltier than the Pacific in order to predict the fate of the MOC under global climate change. The Atlantic salinity is determined by the transport of freshwater both by the atmosphere (through  $E - P$ ) and by

the ocean, and the relative importance of each is unclear. Even if atmospheric transport were the most important factor today, this may change in the future because of greenhouse gas forcing (Seager et al. 2010, 2014). Our work will be useful in understanding future climates and may elucidate the role of the MOC in past climates, when the distribution of  $E - P$  was different from today (Hewitt et al. 2003).

In this study, we focus on one of the more obvious asymmetries between the Atlantic and the Pacific: the difference in basin widths. Specifically, we examine the consequences of this geometrical asymmetry on the oceanic flow and its repercussions on the salinity distribution. The impacts of atmosphere-only processes or atmosphere–ocean feedbacks on the asymmetry in salinity distribution between the basins have been examined using ocean–atmosphere models (e.g., Ferreira et al. 2010; Nilsson et al. 2013). These processes are excluded here by applying fixed surface forcings.

Few studies on the location of deep-water formation have considered the role of the wind-driven gyres. Warren (1983) attributes low salinities in the North Pacific to the small rate of northward flow between the subtropical and subpolar gyres, but he does not consider a scenario with deep-water formation in the North Pacific. Observations show a salinity increase in the North Atlantic correlated with the decreased strength of the subpolar gyre (SPG) during the period from 1965 to 2003 (Hátún et al. 2005; Häkkinen and Rhines 2004).

In this study, we advance an additional mechanism for why the AMOC is preferred to the PMOC, based on the relative strengths of the western boundary currents associated with the MOC and with the SPG in the basin where sinking occurs. An important result relevant for this work is that the transport of the MOC is essentially independent of the sinking location (Jones and Cessi 2016). This is because the MOC transport is determined by three sources: the northward Ekman transport entering the basins from the Southern Ocean, minus the southward eddy thickness transport exiting the same region, plus the global diapycnal upwelling into the upper branch of the MOC. All these sources add up to the total sinking, regardless of its location.

Upon entering the sinking basin, the northward flow of the upper branch of the MOC forms a western boundary current, with a velocity that is independent of the sinking location. This western boundary current is superimposed on the western boundary current associated with the wind-driven gyres. Although the Sverdrup interior meridional velocity in the SPG is the same in both basins, for zonally uniform winds, the western boundary current and the gyre’s zonal velocity are faster

in a wider basin. In the simplified geometry presented here, the MOC northward velocity is larger than the southward SPG western boundary current in the narrow basin (with width similar to the Atlantic) but not in the wide basin (with width similar to the Pacific). The net result is that salty water from the subtropical gyre is carried into the western portion of the SPG when sinking occurs in the narrow basin but not when sinking occurs in the wide basin. Instead, in the wide basin, the southward western boundary current in the SPG brings freshwater from the far north, where the freshwater flux is maximum. The resulting fresh pool suppresses local deep-water formation, and the faster zonal velocity efficiently spreads the freshwater eastward, causing the water in the SPG of the wide basin to become fresher than the water in the SPG of the narrow basin. This process, diagnosed in the 3D model experiments, is documented in section 2.

In section 3, a 2D advection–diffusion model of the upper branch of the MOC is used to explore the salinity distribution for various flow fields and zonal arrangements of deep-water formation. Further idealized experiments with the same 2D model show that neither the MOC western boundary current alone nor the wind-driven gyres alone can produce different salinity fields based on the basin width. However, salt advection by the combined velocity fields, and the associated feedback on deep-water formation, selects the narrow basin as the preferred deep-water mass formation site. Section 4 provides a summary and draws conclusions.

## 2. 3D model and diagnostics

We use a 3D primitive equation version of the MITgcm. The domain consists of two boxes of different widths connected by a reentrant channel occupying the southernmost  $17.5^\circ$  of latitude (Fig. 1). The bottom of the basin is flat and 4000 m deep, except for a sill in the periodic channel, one-grid point wide and 1333 m high, located immediately south of the narrow basin's western boundary.<sup>1</sup> The continents that separate the basins are one-grid point wide and have the same length, extending from  $-52.5^\circ$  to  $70^\circ$ . The equation of state is linear, with the buoyancy described by

$$b = g[\alpha_T T - \beta_S(S - S_{\text{ref}})], \quad (1)$$

where  $\alpha_T = 2 \times 10^{-4} \text{ }^\circ\text{C}^{-1}$ ,  $\beta_S = 7.4 \times 10^{-4}$ , and  $S_{\text{ref}} = 35$ . Salinity  $S$  is given on the practical salinity scale and is

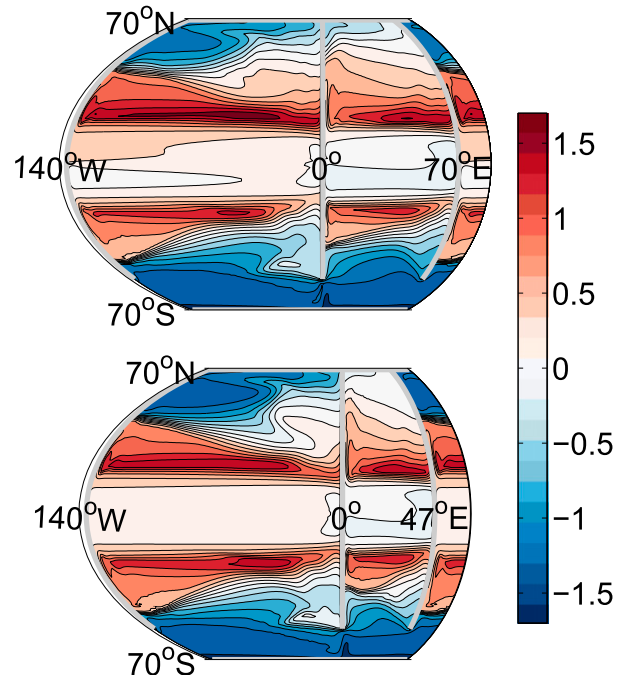


FIG. 1. Surface salinity anomaly, referenced to 35 psu, for zonally symmetric surface forcing in the (top) W2N geometry and (bottom) W3N geometry. Thick gray lines represent boundaries. Contours are every 0.2 psu. The domain is periodic and the western  $20^\circ$  of the domain are repeated to the right of the figure.

therefore presented without units. Temperature  $T$  is in degrees Celsius.

The model is forced at the surface by zonally uniform wind stress  $\tau$ , freshwater flux  $F$ , and temperature relaxation to a profile  $T^*$  given by

$$\tau = \tau_{\text{Max}}[-\cos(3\pi\theta/140) + e^{-\theta^2/\sigma^2}], \quad (2)$$

$$F = F_s[\cos(7\pi\theta/8\Theta) - 2e^{-(\theta/\Theta)^2/(2\sigma_F^2)}] - F_0, \quad \text{and} \quad (3)$$

$$T^* = T_{\text{eq}}[\cos(\pi\theta/140)^2 + 0.1e^{-(\theta/2\Theta-1)^2}], \quad (4)$$

where  $\theta$  is latitude in degrees,  $\tau_{\text{Max}} = 0.1 \text{ N m}^{-2}$ ,  $\sigma = 10^\circ$ ,  $F_s = 2 \times 10^{-8} \text{ m s}^{-1}$ ,  $\sigma_F = 0.128$ ,  $\Theta = 60^\circ$ , and  $T_{\text{eq}} = 25^\circ\text{C}$  (see Fig. 2). The relaxation time scale for the surface temperature is 10 days. The constant  $F_0$  is chosen so that the net freshwater flux into the ocean is zero. The freshwater flux is multiplied by the negative reference salinity  $-S_{\text{ref}}$  in order to obtain the salinity flux into the ocean.

Baroclinic eddies are parameterized using the Gent–McWilliams advective form (Gent and McWilliams 1990) and Redi (1982) isopycnal tracer mixing with equal mixing coefficients  $\kappa_{\text{GM}} = 500 \text{ m}^2 \text{ s}^{-1}$ . The Gent–McWilliams scheme (GM) is implemented using the boundary-value problem framework described by Ferrari et al. (2010). The Redi tensor is tapered to

<sup>1</sup> The W2N experiment described here was repeated with sills at the end of both of the continents and this led to no qualitative changes to the overturning.

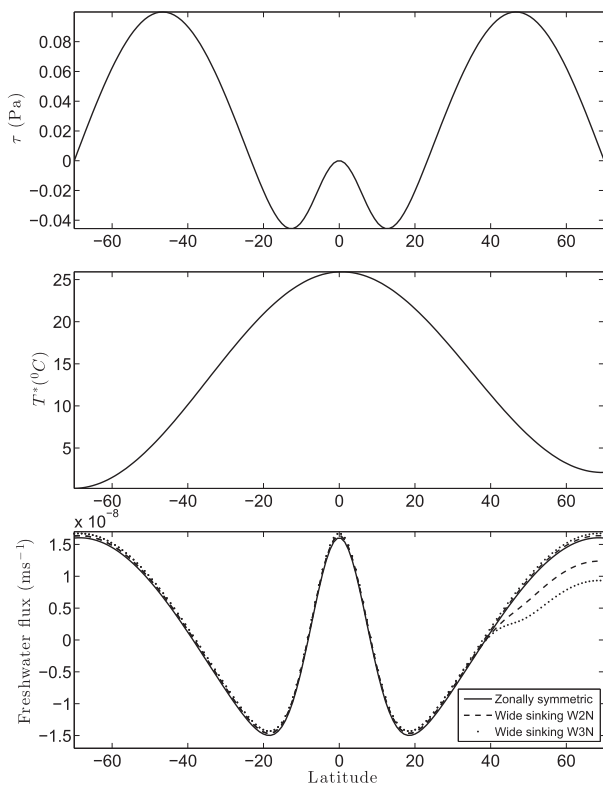


FIG. 2. (top) Surface wind stress (Pa), (middle) profile of temperature used for temperature relaxation ( $^{\circ}$ C), and (bottom) surface freshwater flux forcing ( $\text{m s}^{-1}$ ). The dashed lines show the freshwater flux used to induce sinking in the wide basin in the W2N geometry, and the dotted lines show the freshwater flux used to induce sinking in the wide basin in the W3N geometry. Where these lines split, the upper dashed-dotted line is applied to the narrow basin and the lower one is applied to the wide basin. For wide sinking, the wide-basin freshwater flux is reduced by 0.06 Sv in the W2N geometry and by 0.1 Sv in the W3N geometry.

horizontal diffusion in regions of weak stratification, as described by Danabasoglu and McWilliams (1995). The vertical diffusivity is set to  $2 \times 10^{-5} \text{ m}^2 \text{s}^{-1}$  in the interior, tapering to  $10^{-2} \text{ m}^2 \text{s}^{-1}$  at the surface over a depth of 20 m to model the mixed layer. Each simulation was run for at least 3000 years, until equilibrium was reached. Additional details of the model configuration are given in Jones and Cessi (2016).

Two configurations are considered in the 3D model: one in which the wide basin is twice as wide as the narrow basin (W2N) and one in which the wide basin is 3 times as wide as the narrow basin (W3N). These geometries are shown in Fig. 1, together with the surface salinity obtained under zonally uniform surface forcing; in both geometries, the wide basin is 140° wide, with the narrow basin 70° wide for W2N and 47° wide for W3N. Under zonally uniform forcing, deep-water formation occurs in the narrow basin only, regardless of the initial

condition, and the surface salinity in the SPG of the narrow basin is higher for W3N than for W2N.

Sinking in the wide basin can be coerced by reducing the freshwater flux at the northern end of the wide-basin sector, while compensating this reduction by a uniform freshwater flux increase everywhere else. A larger asymmetry in freshwater flux is needed to force wide sinking in the W3N geometry than in the W2N geometry (see the bottom panel of Fig. 2), suggesting that the larger the ratio of basin widths, the greater the preference for narrow sinking. For both W2N and W3N, the wide sinking state reverts to narrow sinking when the forcing is slowly (over 20 000 years) returned to zonal symmetry. In summary, wide sinking is unstable under zonally uniform freshwater forcing.

We frame the discussion of the meridional transport in terms of the residual overturning circulation (ROC) rather than the Eulerian circulation. The ROC is defined as the time and zonally averaged meridional transport at constant buoyancy rather than at fixed depth levels. Thus, it measures the transport of buoyancy rather than the transport of volume. The ROC is more representative of the transport of tracers than the Eulerian transport (Andrews and McIntyre 1978). The ROC streamfunction is defined as

$$\psi(y, \tilde{b}) = \frac{1}{T} \int_0^T \int_0^{L_x} \int_{-H}^0 v \mathcal{H}[b(x, y, z, t) - \tilde{b}] dz dx dt, \quad (5)$$

where  $v$  is the Eulerian plus parameterized eddy velocity,  $H$  is the total depth,  $L_x$  is the width of the basin,  $T$  is the averaging time scale (100 yrs is chosen here), and  $\mathcal{H}$  is the Heaviside function. The ROC streamfunction  $\psi$  is the zonally integrated transport of water above  $b = \tilde{b}$ . In Figs. 3 and 4 (filled color contours), the ROC streamfunction is remapped into  $z$  coordinates using the zonal-mean isopycnal height, which is defined as

$$\mathcal{Z}(y, \tilde{b}) = -\frac{1}{T} \int_0^T \frac{1}{L_x} \int_0^{L_x} \int_{-H}^0 \mathcal{H}[b(x, y, z, t) - \tilde{b}] dz dx dt. \quad (6)$$

In  $z$  coordinates, it is useful to define the modified buoyancy  $b^\#(y, z)$ , where  $\mathcal{Z}[y, b^\#(y, z)] = z$ . The field  $b^\#$  is advected by the ROC streamfunction  $\psi$ , and thus  $\psi$  is constant on  $b^\#$  contours for adiabatic flow. In Figs. 3 and 4, contours of  $b^\#$  show the stratification: isopycnals outcropping in the north of the sinking basin also outcrop in the channel, and flow parallel to these contours is adiabatic below the mixed layer. Because of longitudinal buoyancy gradients, the zonally averaged remapping [(6)] distorts the vertical extent of the mixed layer. Values of  $b^\#$  higher than  $40 \times 10^{-3} \text{ m s}^{-2}$  are not plotted because the contours would be too close together.

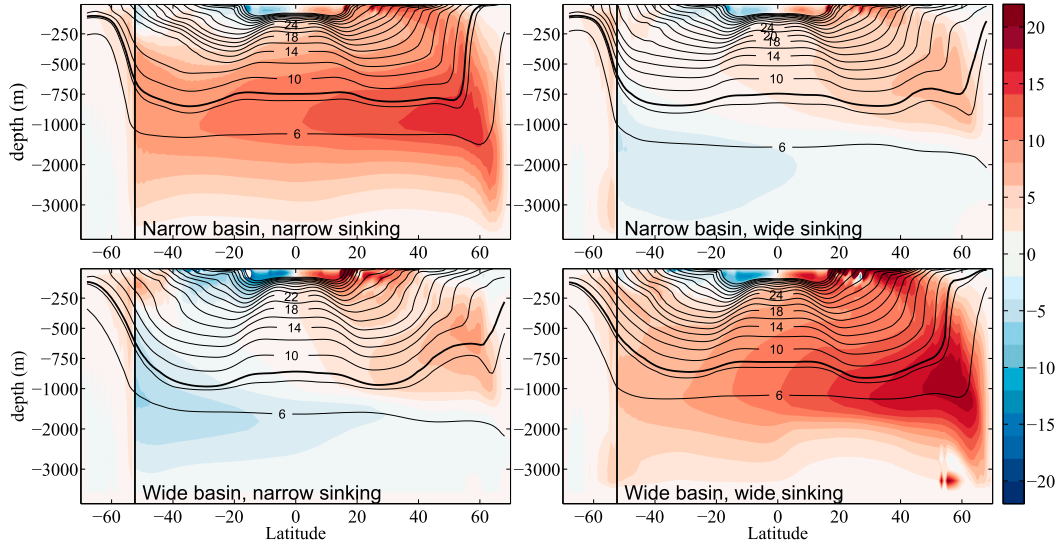


FIG. 3. Residual overturning streamfunction ( $\text{Sv}$ ; color shading; spacing  $2 \text{ Sv}$ ), and  $b^{\#} \times 10^3 \text{ m s}^{-2}$ , the buoyancy of the surface whose average depth is  $\mathcal{Z}$  (black contours) in the (top) narrow basin and the (bottom) wide basin with (left) narrow sinking and (right) wide sinking for the W2N geometry. In all plots, the reentrant channel region (left of the thick black vertical line) shows the total streamfunction integrated over all longitudes. The thick black contour denotes the isopycnal  $b_m = 0.0085 \text{ m s}^{-2}$ , which bounds the upper branch of the MOC from below.

The buoyancy value  $b_m = 0.0085 \text{ m s}^{-2}$  (thick black line in Figs. 3 and 4) is chosen to divide the upper and lower branches of the overturning. In practice, this isopycnal contour is chosen to pass as close as possible through the maxima of both the deep overturning cell in the sinking basin and the shallow overturning cell in the nonsinking basin. The upwelling across this isopycnal contour is approximately fixed by wind stress in the Southern Ocean (plus eddy transport of buoyancy) and global diapycnal diffusion (Gnanadesikan 1999; Allison 2009;

Jones and Cessi 2016), setting the cross-equatorial northward transport of the upper branch of the MOC in the sinking basin to approximately  $11 \text{ Sv}$  regardless of the location of sinking (Fig. 5, red lines). This cross-equatorial transport, augmented by the diapycnal upwelling across  $b_m$  in the Northern Hemisphere of the sinking basin, determines the maximum transport of the MOC.

In the nonsinking basin, diffusive upwelling feeds a shallow cell in the Northern Hemisphere and an abyssal cell (mostly in the Southern Hemisphere). The upwelled

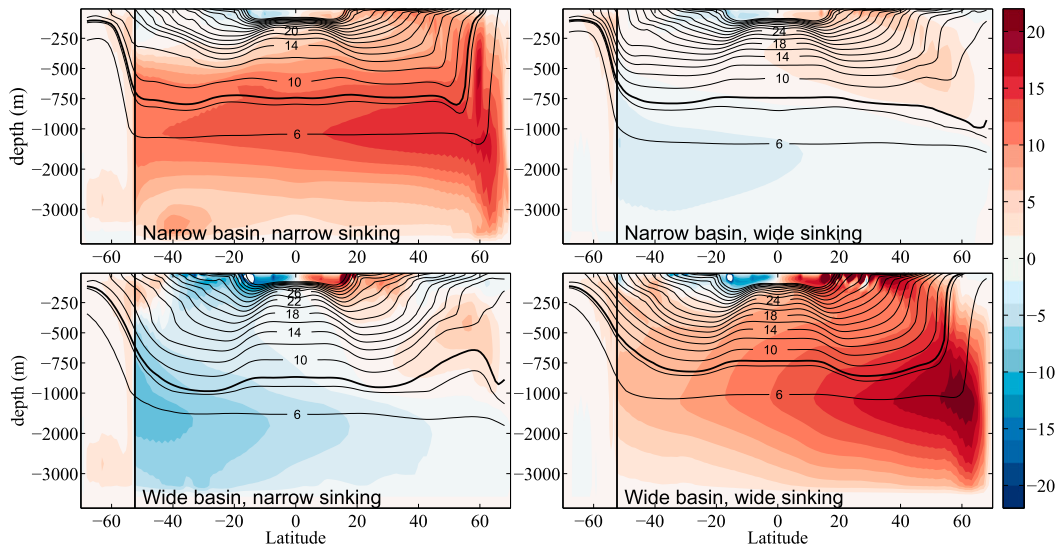


FIG. 4. As in Fig. 3, but for the W3N geometry.

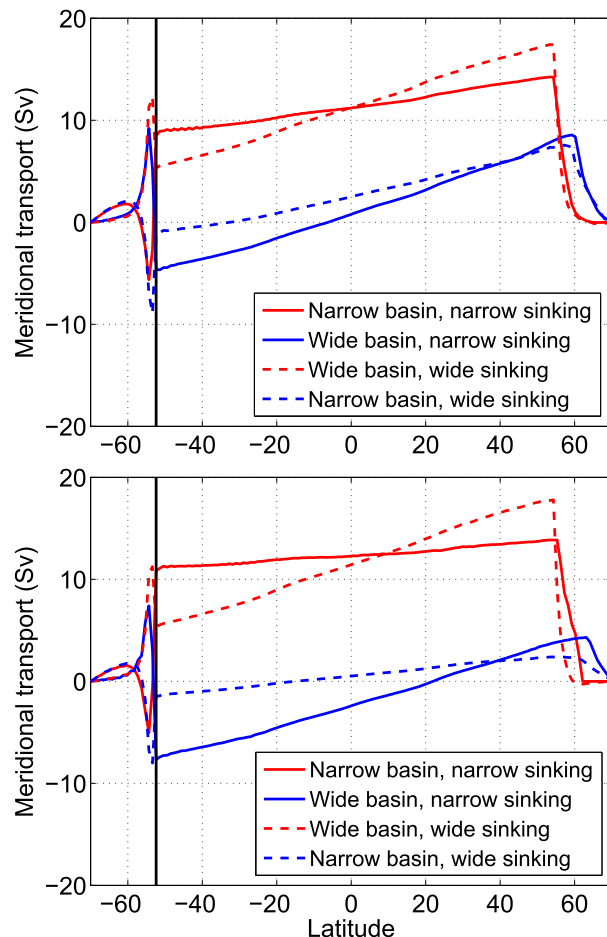


FIG. 5. Meridional transport, zonally and vertically integrated within each sector above the isopycnal  $b_m$  for (top) W2N and (bottom) W3N.

water flows northward, sinking to about 1000 m at high northern latitudes, and then returns southward. The meridional transport in the nonsinking basin integrated zonally and above  $b_m$  is shown in Fig. 5 (blue lines).

The numerical simulations indicate why wide sinking is unstable when the surface freshwater flux is symmetric: Fig. 6 (top panels) shows the salinity zonally and vertically averaged above  $b_m$ . The values in the sinking region of the wide basin (red dashed lines in the gray box of Figs. 6 and 7) are only slightly above the values in the narrow, nonsinking basin at the same latitudes (blue dashed lines in the gray box of Figs. 6 and 7); this is despite the decreased surface freshwater flux in the wide basin relative to the narrow basin. In other words, it appears that it is the zonal asymmetry in freshwater forcing that keeps the wide basin slightly saltier than the narrow basin. Without this asymmetry, the salinities of the basins reverse and narrow sinking occurs.

To quantify how the salinity might be distributed under zonally uniform forcing for wide sinking, we

advect and diffuse a passive tracer with the velocity, diffusivity, and convective adjustment time series from the wide sinking state. Unlike salt, the tracer is forced with the zonally uniform surface flux given by the solid line in Fig. 2. The resulting tracer field vertically averaged above  $b_m$  is shown in the bottom panel of Fig. 8. Compared to the salinity anomaly (middle panel of Fig. 8), the tracer is lower in the wide basin and higher in the narrow basin and comparable to the values encountered in the narrow sinking case (top panel of Fig. 8). To make a more quantitative comparison between the three cases, it is useful to examine the salinity and tracer concentrations averaged above  $b_m$  and then zonally averaged. Figure 6 shows that, for wide sinking, the tracer concentration anomaly at the latitudes of sinking is larger in the narrow basin than in the wide basin (cf. the dashed lines in the gray box in the bottom panels of Fig. 6).

At high latitudes, the temperature is approximately independent of the location of sinking and thus does not contribute directly to the preference for narrow over wide sinking. However, at the sinking latitudes, the temperature of the sinking basin is slightly higher than the temperature of the nonsinking basin, so it partially counteracts the effects of salinity on the buoyancy. Consequently, when the salinity in the sinking region is only marginally larger than the salinity in the nonsinking basin, the negative temperature advection feedback destabilizes the wide sinking state.

The buoyancy is displayed in the top panels of Fig. 7, vertically averaged above the isopycnal  $b_m$ , and then zonally averaged. For wide sinking, the buoyancy in the sinking region is lower than at the same latitudes of the narrow basin (cf. the dashed lines in the gray box in the top panels of Fig. 7); wide sinking is obtained under zonally asymmetric forcing. In the bottom panels of Fig. 7, the symmetrically forced tracer is used instead of the salinity to find “tracer buoyancy,” that is, the hypothetical buoyancy obtained if wide sinking occurred with zonally uniform salinity forcing. For wide sinking, the tracer buoyancy at high latitudes is indeed lower in the narrow basin than in the wide basin (cf. the dashed lines in the gray box in the bottom panels of Fig. 7). This confirms that the wide sinking solution is unstable under zonally uniform surface salt flux forcing.

Salinity in turn affects the distribution of convective adjustment,<sup>2</sup> which is rather different for narrow and wide sinking. Convective adjustment is the main process determining the diapycnal velocity across the buoyancy

<sup>2</sup> In this 3D model, convection is parameterized by convective adjustment: when the stratification is unstable, the vertical diffusivity is increased to  $\kappa_v = 10 \text{ m}^2 \text{s}^{-1}$  until the buoyancy profile becomes stable.

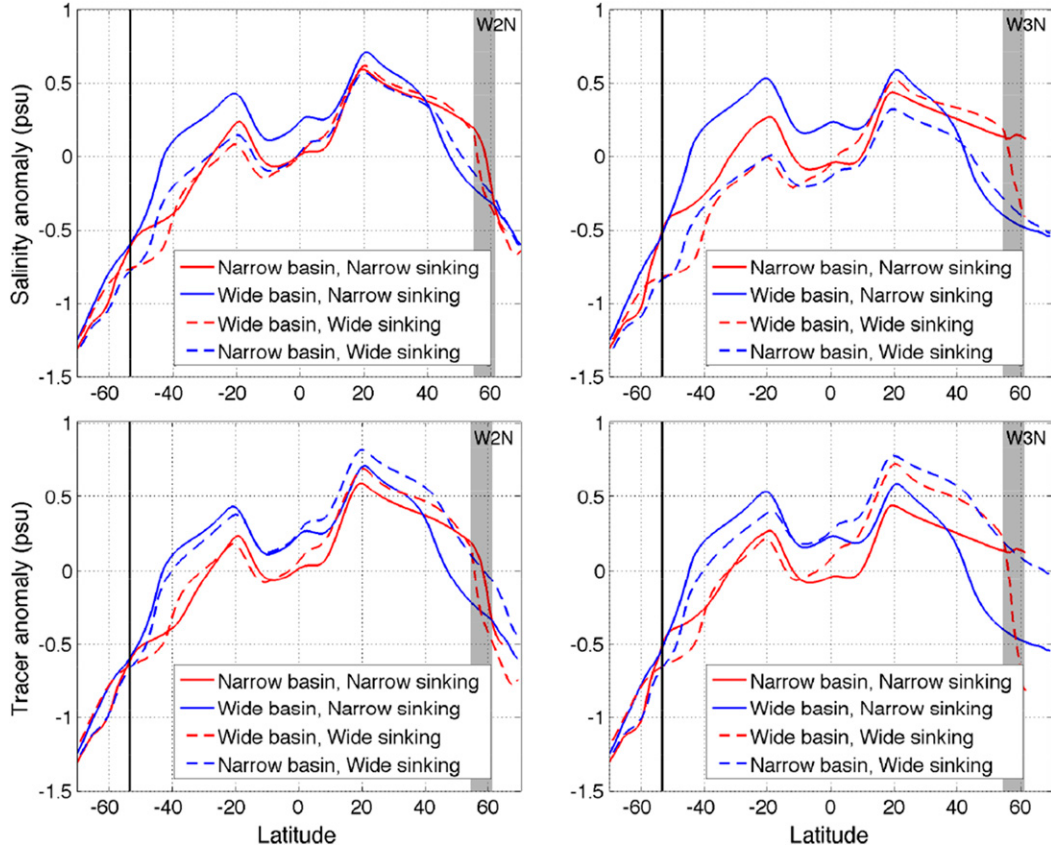


FIG. 6. (top) The depth and zonally averaged salinity anomaly (referenced to 35 psu) above  $b_m = 0.0085 \text{ m s}^{-2}$  and (bottom) the depth and zonally averaged tracer anomaly above  $b_m = 0.0085 \text{ m s}^{-2}$  for (left) W2N and (right) W3N. The solid lines are for narrow sinking, and the dashed lines are for wide sinking. The gray box marks the location of sinking.

$b_m$ . Thus, we use the diapycnal velocity, denoted with  $\varpi/b_z$  following the notation of Young (2012), henceforth referred to as WRY12, as a measure of deep-water formation. As illustrated in Fig. 9,  $\varpi/b_z$  occurs predominantly at the northern end of the sinking basin. For wide sinking,  $\varpi/b_z$  is confined to the eastern two-thirds of the domain, whereas for narrow sinking, it is spread throughout the whole width of the basin. This pattern reflects the zonal distribution of salinity (cf. Figs. 9 and 8). In the western third of the wide sinking basin, the surface is especially fresh, while it is relatively salty almost everywhere in the narrow sinking basin.

We now demonstrate that the contrast in the zonal distribution of salinity results from differences in the velocities near the western boundary of the sinking basin. As shown in Fig. 10, for narrow sinking, the western boundary current is northward in the narrow basin south of about  $57^\circ$ . North of  $57^\circ$  the velocity is near zero. For wide sinking, the velocity on the western boundary of the wide basin is southward north of  $45^\circ$  and northward south of  $45^\circ$ ; that is, the change of sign of the western boundary current

coincides with the boundary between the subtropical gyre and the SPG. Therefore, salinity is transported farther north into the western portion of the SPG for narrow sinking. The resulting high salinity in the narrow basin enables deep convection (Fig. 9, top panel). In the north of the wide basin, deep-water formation is suppressed on the western side of the SPG by the low salinities carried southward by the western boundary current, and the isopycnal  $b_m$  does not outcrop there (Fig. 9, bottom panel).

The western boundary velocity in the sinking basin is the sum of the northward flow of the MOC plus the western boundary current associated with the locally wind-driven Sverdrup gyre, which is northward in the subtropical gyre and southward in the SPG. For the W2N geometry, the Sverdrup transport of the SPG at  $58^\circ$  (halfway between the zero-wind stress curl line and  $70^\circ$ ) is about 30 Sv in the wide basin and about 15 Sv in the narrow basin, as shown in Fig. 12. This interior transport produces a southward western boundary current in the SPG, which is twice as fast in the wide basin than in the narrow basin. The zonal velocity associated

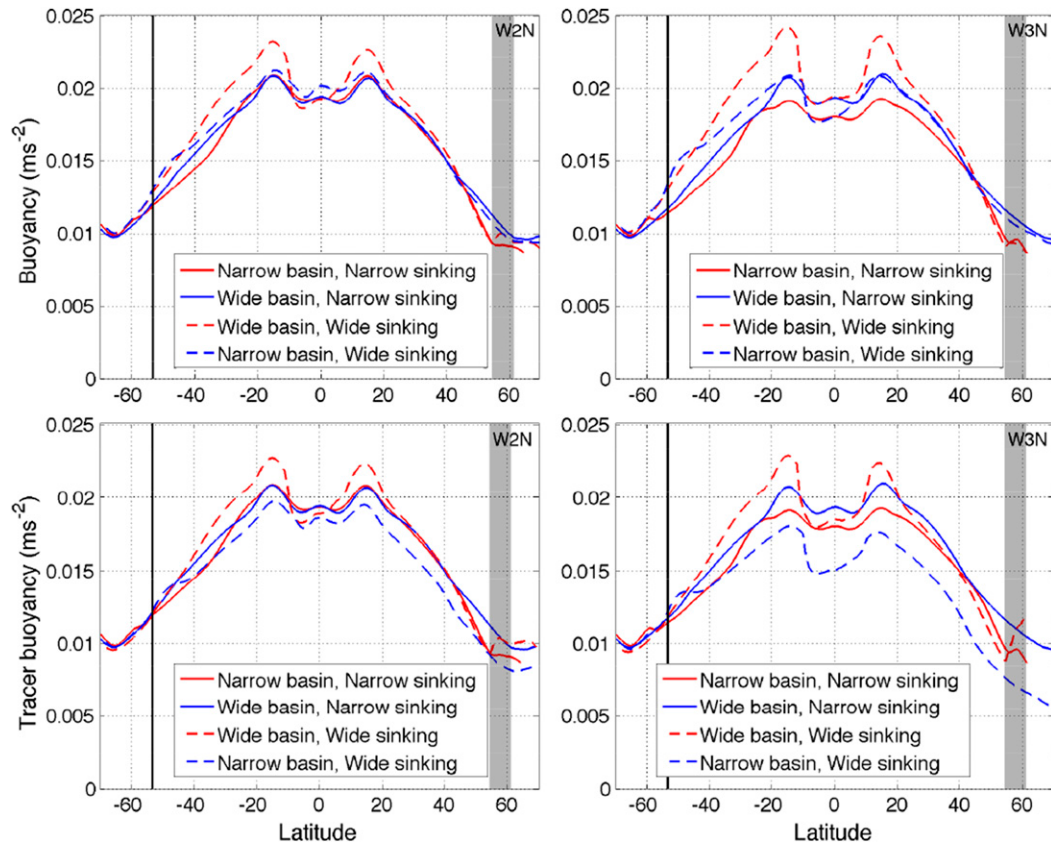


FIG. 7. The zonally averaged buoyancy averaged above  $b_m = 0.0085 \text{ m s}^{-2}$  (top) using the salinity and (bottom) using the passive tracer instead of salinity for (left) W2N and (right) W3N. For tracer buoyancy, the depth of  $b_m$  is still calculated using the salinity. The solid lines are for narrow sinking, and the dashed lines are for wide sinking. The gray box marks the location of sinking.

with the Sverdrup gyre is also faster in the wide basin. However, the MOC transport, largely confined to a western boundary current within each basin, is about 15 Sv, independent of the width of the sinking basin. The total flow above  $b_m$  is approximately a linear combination of the gyres and the MOC western boundary current (Stommel 1957). The MOC velocity is of similar amplitude to the SPG western boundary current in the narrow basin and in the opposite direction, but it is half of the velocity of the SPG western boundary current in the wide basin. As a result, the western boundary current is strong and southward in all the SPG of the wide basin but not in the narrow basin (as shown in Fig. 10). The difference in velocities on the western side of the basins leads to different salinity distributions in the SPG region: fresher in the wide sinking basin than in the narrow sinking basin. The halocline that forms on the western side of the wide basin suppresses deep-water formation, localizing the diapycnal velocity to the eastern side of the wide basin. This localization, given a zonally uniform freshwater flux, reduces the efficiency

of the salt feedback on water mass formation in the wide basin, giving a preference to narrow-basin sinking. To further demonstrate this process, in the following section we examine the salinity distribution obtained with zonally uniform freshwater fluxes and velocities that are simplified relative to the full 3D field.

### 3. 2D model and diagnostics

To understand the role of the epicycinal and diapycnal velocity in the salinity distribution, we simplify the salinity equation in three dimensions. The MITgcm solves the three-dimensional advection–diffusion equation:<sup>3</sup>

$$\frac{\partial S}{\partial t} + (uS)_x + (vS)_y + (wS)_z = \nabla \cdot (\mathbf{K} \nabla S) + (\kappa_v S_z)_z, \quad (7)$$

<sup>3</sup> In this section, we use Cartesian coordinates, but the actual computations are in the spherical coordinates appropriate for the sector shown in Fig. 1.

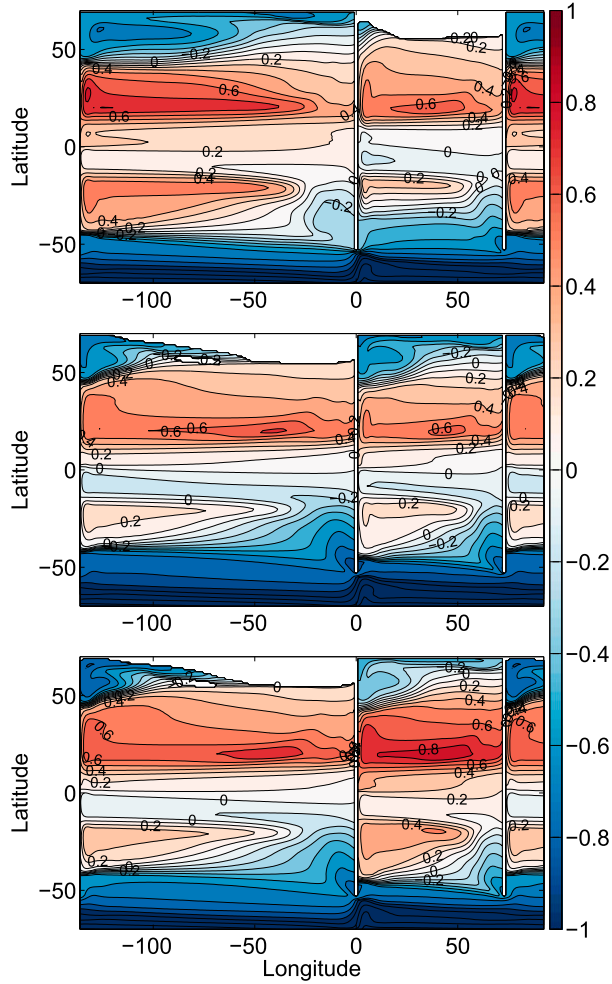


FIG. 8. Salinity anomaly, referenced to 35 psu, vertically averaged above the isopycnal  $b_m = 0.0085 \text{ m s}^{-2}$  for (top) narrow sinking and (middle) wide sinking in the W2N geometry. (bottom) Anomaly of the tracer advected and diffused as for wide sinking, vertically averaged over the same depth range as the middle panel. The isopycnal  $b_m$  outcrops in the white area.

where  $S$  is the salinity, and  $(u, v, w)$  is the Eulerian plus GM velocity in the  $(x, y, z)$  direction, respectively;  $\mathbf{K}$  is the Redi (1982) tensor defined in (A2), and  $\kappa_v$  is the vertical diffusivity.

A reduced description is obtained by integrating (7) vertically from the buoyancy surface  $b_m$  to the sea surface and changing to buoyancy coordinates  $(\tilde{x}, \tilde{y}, \tilde{b}, \tilde{t})$ , following WRY12 (details are in appendix A). Making the further assumption that  $S$  is vertically homogeneous above  $b_m$ , we obtain

$$\begin{aligned} & (-\zeta \bar{S})_{\tilde{t}} + (U \bar{S})_{\tilde{x}} + (V \bar{S})_{\tilde{y}} - \frac{\varpi}{b_z} S \Big|_{\zeta} \\ &= -(\zeta \kappa_{GM} \bar{S}_{\tilde{x}})_{\tilde{x}} - (\zeta \kappa_{GM} \bar{S}_{\tilde{y}})_{\tilde{y}} - F S_{ref} - \kappa_v S_z \Big|_{\zeta}, \quad (8) \end{aligned}$$

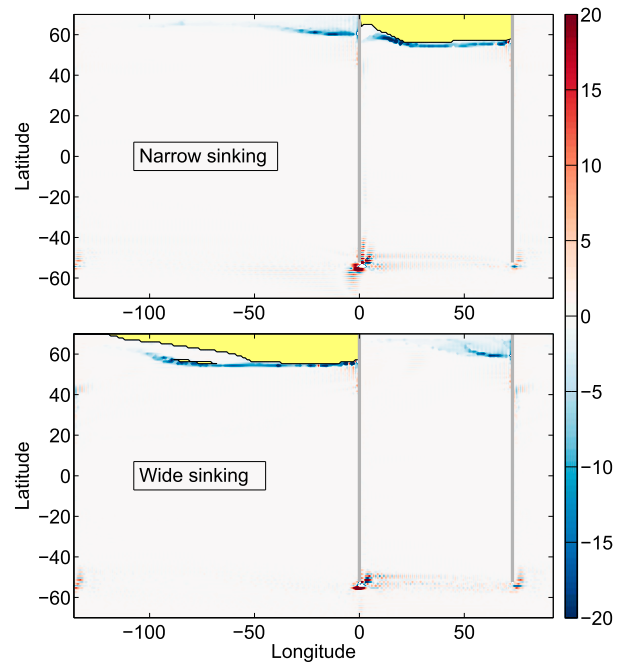


FIG. 9. The diapycnal velocity  $\varpi/b_z \times 10^6 \text{ m s}^{-1}$  at isopycnal  $b_m = 0.0085 \text{ m s}^{-2}$  from the 3D model for (top) narrow sinking and (bottom) wide sinking in the W2N geometry. The isopycnal  $b_m$  outcrops in the yellow area.

where  $\kappa_{GM}$  is the Redi diffusion coefficient (here taken to be equal to the GM eddy diffusivity),  $U = \int_{\zeta}^0 u dz$  and  $V = \int_{\zeta}^0 v dz$  are the sum of Eulerian plus GM velocities depth integrated above  $b_m$ ,  $\bar{S}$  is the salinity depth averaged above  $b_m$ , and  $\zeta(\tilde{x}, \tilde{y})$  is the time-averaged depth of the isopycnal  $b_m$ . We further assume

$$S|_{\zeta} = \bar{S}, \quad S_z|_{\zeta} = \frac{\bar{S}}{-\zeta}. \quad (9)$$

The 2D model is now exploited to more deeply understand the mechanisms that determine the salinity distribution, using the vertically integrated velocity field, which satisfies the incompressibility condition in buoyancy coordinates ( $\zeta$  is assumed to be independent of time):

$$U_{\tilde{x}} + V_{\tilde{y}} = \frac{\varpi}{b_z}. \quad (10)$$

#### a. Vertically integrated velocities from in the 3D model

We obtain  $U$  and  $V$  by integrating the residual velocities in the 3D W2N geometry vertically above  $b = b_m$ . The quantity  $\zeta$  is the associated time-mean depth of the isopycnal  $b_m$ , and  $\varpi/b_z$  is obtained from (10). Unlike the 3D salinity computations, here the freshwater flux is zonally uniform for both narrow and wide sinking, just as in the passive tracer experiments described in the previous

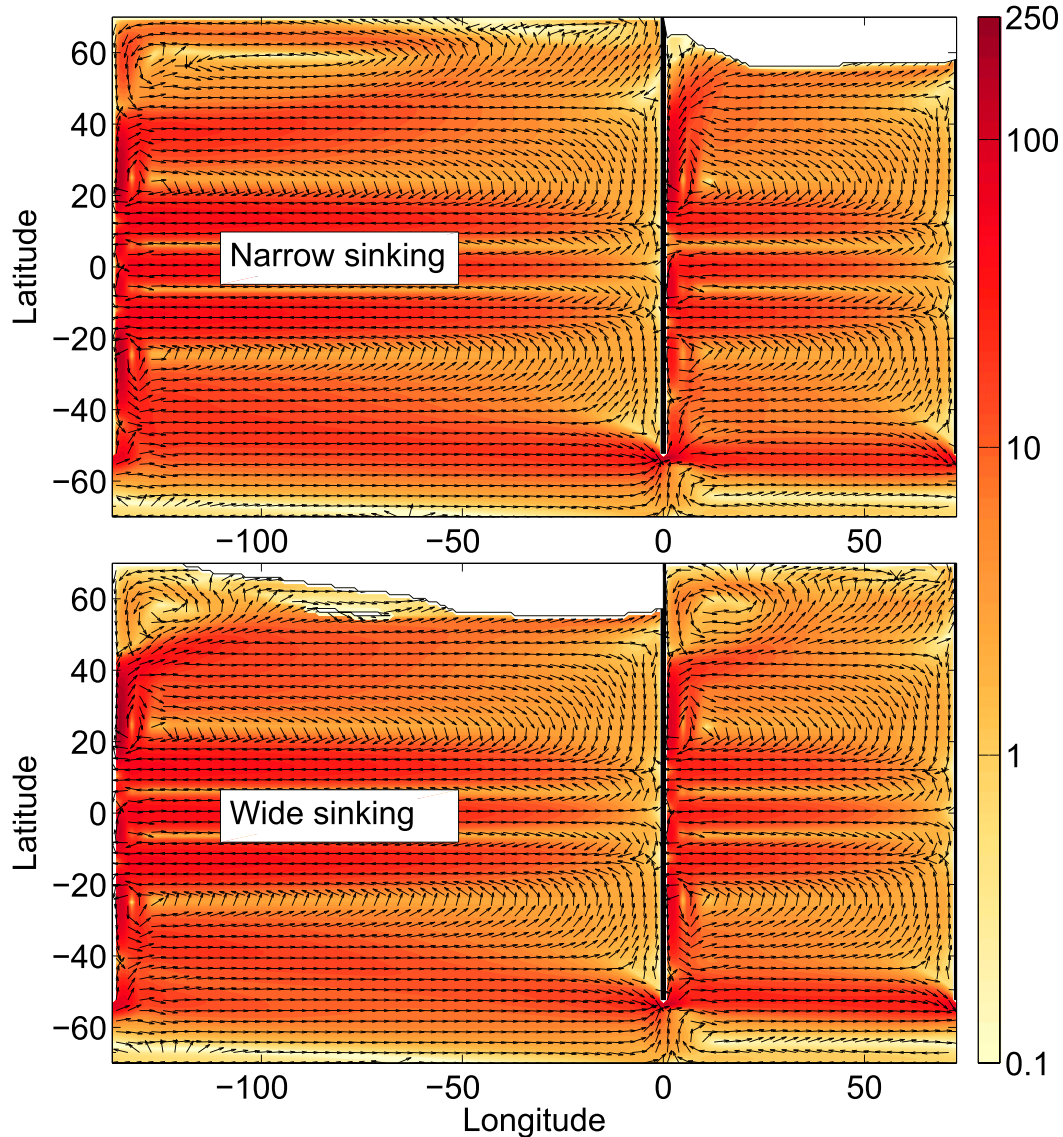


FIG. 10. Magnitude (color) and direction (arrows) of the mean plus GM velocity vertically integrated above isopycnal  $b_m = 0.0085 \text{ m s}^{-2}$  for (top) narrow sinking and (bottom) wide sinking. Each arrow represents the mean direction over a  $3^\circ \times 3^\circ$  box while the magnitude is on the model's grid. The contour color scale is in  $\text{m}^2 \text{s}^{-1}$  and is spaced logarithmically to visualize both boundary and interior currents. The isopycnal  $b_m$  outcrops in the white area.

section. The goal of this 2D experiment is to diagnose which components of the velocities are essential to determine the differences in the salinity distribution between narrow and wide sinking. The  $U, V$  field in the Northern Hemisphere is shown in Fig. 10, and  $\varpi/b_z$  is shown in Fig. 9.

Despite ignoring the baroclinic terms, the 2D salinity obtained with (8) reproduces fairly well some aspects of the 3D computations and in particular the salinity vertically averaged above  $b_m$  (cf. the bottom-left panel of Fig. 6 with Fig. 11a), indicating that the vertically integrated transport dominates the salinity distribution of the upper

branch of the MOC, especially in the subpolar regions. The agreement is less satisfactory in the subtropical regions, where the depth of  $b_m$  is largest: here, the vertical correlation of the baroclinic components dominates the salinity transport (diagnostic not shown). The resulting salinities are higher at the northern end of the SPG in the narrow basin for both narrow and wide sinking velocities (red solid and blue dashed lines in the gray box of Fig. 11a); that is, the 2D model confirms the prediction of the passive tracer 3D computations that narrow sinking is preferred when the freshwater flux is zonally symmetric.

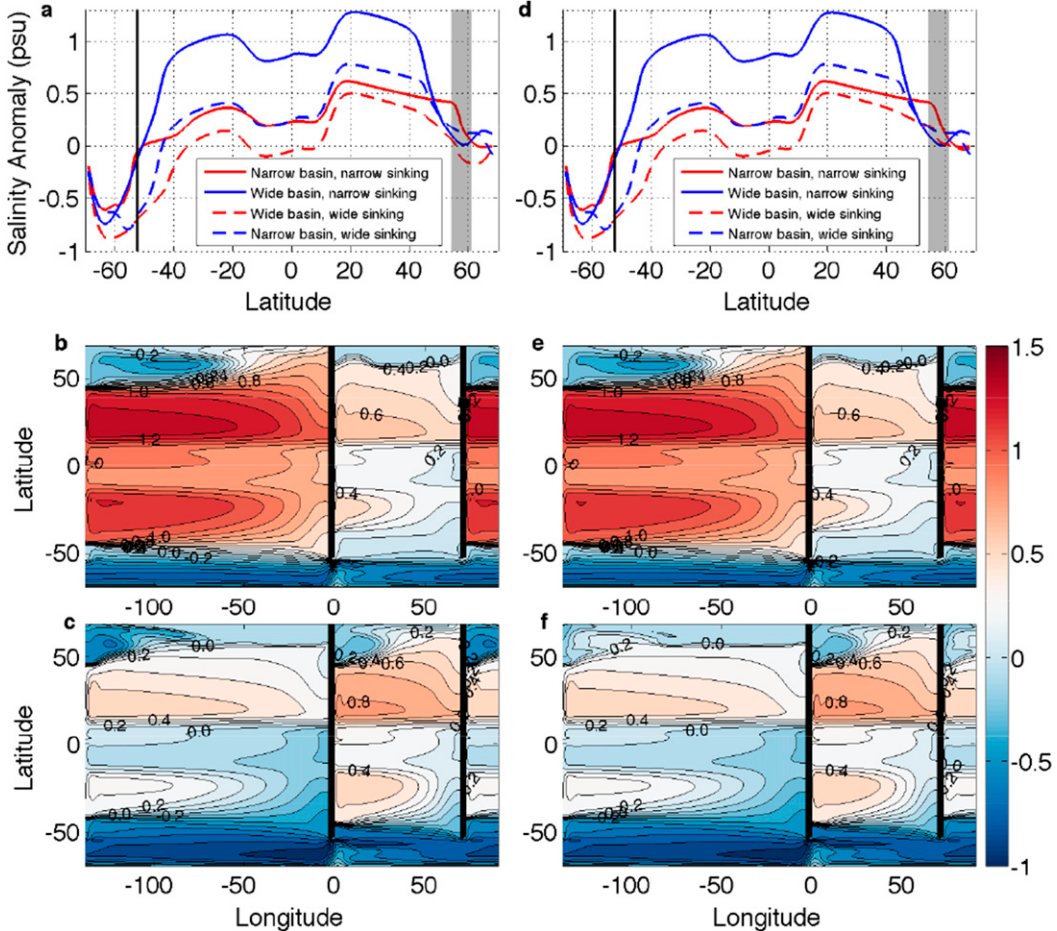


FIG. 11. Salinity anomaly solution of (8) using  $U$ ,  $V$ ,  $w/b_z$ , and  $\zeta$  from the W2N computation (a) zonally averaged and plotted as a function of latitude and longitude for (b) narrow sinking and (c) wide sinking. (d)–(f) As in (a)–(c), but where  $U$  and  $w/b_z$  are modified such that  $w/b_z$  is zonally homogenized in the subpolar gyre of the sinking basin. The depth of the layer  $-\zeta$  is capped so that the minimum depth is 70 m. Contours are every 0.1 psu. The gray box in (a) and (d) marks the location of sinking.

Because the 2D advection–diffusion model [(8)] treats  $\bar{S}$  as a passive scalar, it does not incorporate the salt feedback controlling the onset of convective adjustment in the sinking region and the associated large diapycnal velocity  $w/b_z$ . To demonstrate that the spatial distribution of  $w/b_z$  is important, we conduct an experiment where this spatial distribution is varied.

In the 2D experiment reported in the left panels of Fig. 11, the term  $w/b_z$  extends over the whole width of the basin for narrow sinking, but it is confined to the eastern two-thirds of the basin for wide sinking (as shown in Fig. 9). An additional experiment is carried out where  $w/b_z$  is modified to be zonally uniform in the sinking basin north of  $46^\circ$ , keeping the meridional velocity  $V$  unchanged. The changes in  $w/b_z$  are accommodated by changing the zonal velocity  $U$  so that (10) is satisfied. The zonal integral of  $w/b_z$  is conserved at every latitude in this process, and the velocities outside the SPG of the sinking basin remain unchanged. With advection

by this modified velocity field the sinking wide basin gets saltier (cf. the red dashed lines in Figs. 11a,d) because the freshwater flowing south in the western boundary sinks rather than being advected eastward into the SPG.

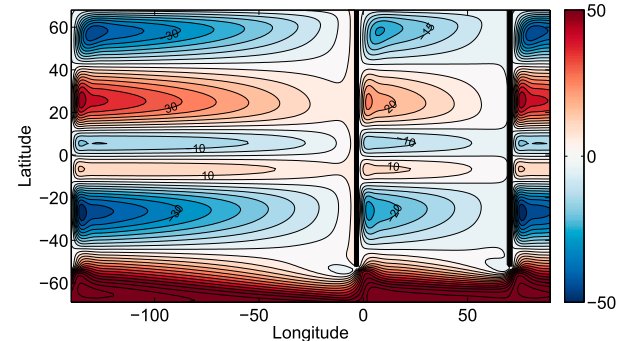


FIG. 12. Streamfunction (Sv) associated with  $U_{\text{gyre}}$  and  $V_{\text{gyre}}$ . Contours are every 5 Sv.

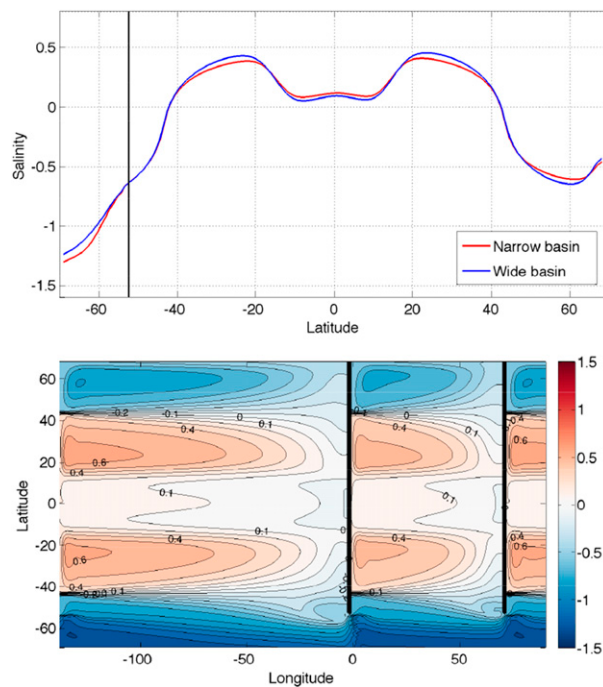


FIG. 13. (top) Zonally averaged salinity anomaly and (bottom) salinity anomaly when (8) uses the velocity associated with the streamfunction in Fig. 12 and  $\zeta = -700$  m with contours every 0.1 psu.

The salinity remains essentially unchanged for narrow sinking (cf. the solid lines in Figs. 11a,d) because  $\varpi/b_z$  is already approximately homogenous for narrow sinking. Therefore, the preference for narrow sinking is reduced when the suppression of convective adjustment by freshening, that is, the salt advection feedback, is removed.

In summary, the salinity in the upper branch of the MOC is controlled by the velocity vertically averaged above the isopycnal  $b_m$  and by the pattern of strong diapycnal velocity because of convective adjustment. The associated deep-water mass formation is suppressed by a halocline on the western side of the wide basin. This latter feedback is not captured by (8), which treats salinity as a passive scalar, but the contrast between the two experiments with the localized versus homogenized  $\varpi/b_z$  illustrates this effect. Both experiments reveal that the velocity field in the SPG is responsible for the halocline formation on the western side of the wide sinking region.

To strengthen our argument that it is the superposition of the SPG velocity plus the MOC's western boundary current that controls the formation of the halocline in the western part of the SPG, we perform two additional experiments with idealized velocities representing either the gyral circulation alone or the MOC circulation alone. Neither of these patterns in isolation lead to the observed differences in SPG salinities.

### *b. 2D advection–diffusion of salinity with idealized velocities*

In the following, we show that, in isolation, neither the gyral velocities alone nor the MOC velocity alone can lead to a halocline in the wide-basin SPG.

We first show the salinity distribution with advection by idealized vertically integrated velocities  $U_{\text{gyre}}$  and  $V_{\text{gyre}}$  representing the gyres in the 2D model. The fields  $U_{\text{gyre}}$  and  $V_{\text{gyre}}$  are found by solving the 2D primitive equations in a domain with W2N geometry, uniform buoyancy, depth of 700 m, and wind forcing  $\tau$ . Two ridges, one south of the continent at  $0^\circ$  with height 280 m and one south of the continent at  $70^\circ\text{E}$  with height 140 m, are included in order to keep the circumpolar transport comparable to that in the 3D simulation. The resulting horizontally nondivergent transport is described by a single streamfunction shown in Fig. 12, and there is neither a diapycnal velocity nor a zonally averaged meridional transport. Figure 13 shows the distribution of the resulting tracer solution of (8), forced by the zonally uniform freshwater flux of Fig. 2. In the along-streamlines direction, the dominant balance is between the isopycnal advection terms and the surface salinity flux. In the across-streamlines direction, the dominant balance is between the isopycnal diffusion terms and the surface salinity flux.

Although the gyres in the wide basin have twice the western boundary current transport compared to the narrow basin, the interbasin salinity difference is minimal: the minimum salinity in the wide basin's SPG is 0.07 psu fresher than the minimum salinity in the narrow basin's SPG (bottom panel of Fig. 13), and the zonally averaged salinities differ very little between basins (top panel of Fig. 13). These differences are too small to explain the preference for narrow sinking seen in the 3D model, and a scale analysis in appendix B confirms that the salinity in this configuration is independent of basin width.

We now examine the salinity distribution with a velocity field characterized by sinking and a western boundary current associated with the MOC without wind-driven gyres. The velocities  $U$ ,  $V$  and  $\varpi/b_z$  in (8) are defined analytically. They are confined to a western boundary current in a single basin fed by upwelling in the periodic channel. In the western boundary current and most of the channel, the dominant balance in (8) is between isopycnal salinity advection and the surface salinity flux. Elsewhere, velocities are very small, so the dominant balance is between isopycnal diffusion and the surface salinity flux. The idealized velocity fields for both narrow and wide sinking are shown in Figs. 14, 15c, and 15d with  $\zeta$  shown in Fig. 15b. The resulting zonally averaged salinities are shown in Fig. 15a: this configuration illustrates that the main effect of the

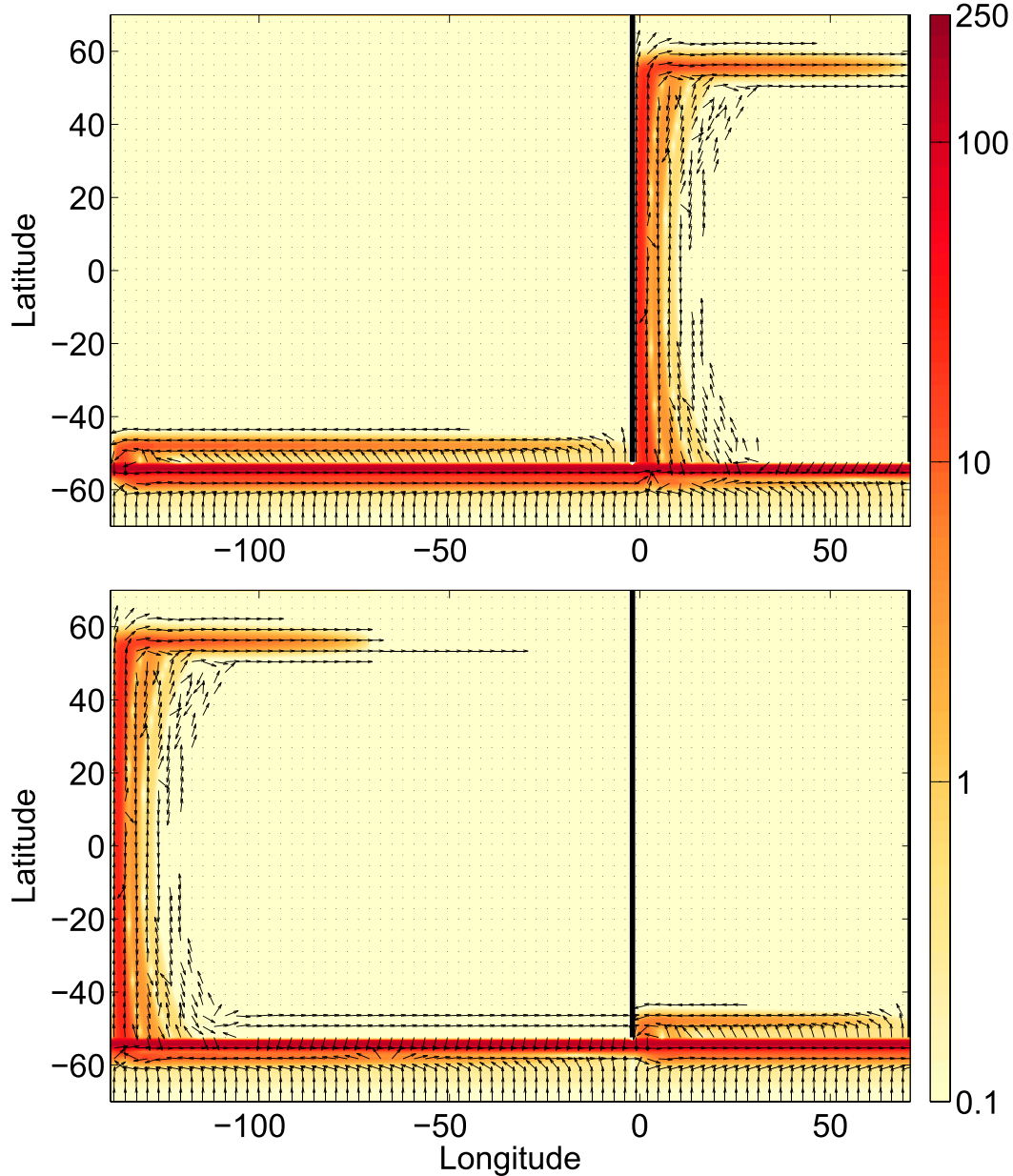


FIG. 14. Magnitude (colors) and direction (arrows) of depth-integrated velocity ( $\text{m}^2 \text{s}^{-1}$ ) in the idealized 2D model for (top) narrow sinking and (bottom) wide sinking. Arrows are not plotted if the magnitude of the depth-integrated velocity is less than  $0.01 \text{ m}^2 \text{s}^{-1}$ . Each arrow represents the mean direction over a  $3^\circ \times 3^\circ$  box while the magnitude is on the model's grid.

Downloaded from [http://journals.ametsoc.org/jpo/article-pdf/47/11/2843/4598889/jpo-d-17-0075\\_1.pdf](http://journals.ametsoc.org/jpo/article-pdf/47/11/2843/4598889/jpo-d-17-0075_1.pdf) by Columbia University user on 27 November 2020

MOC's velocity is to reduce the latitudinal salinity gradients in the sinking basin relative to the nonsinking basin, without privileging narrow versus wide sinking.

#### 4. Conclusions

In a configuration with two basins of different widths connected by a reentrant channel, sinking occurs in the narrow basin under zonally uniform forcing. Deep-water

formation in the wide basin can be coerced by reducing the freshwater flux over the north of the wide basin and then we find that a stronger reduction is needed for larger ratios of basin widths. Despite the reduction in freshwater flux for wide sinking, the salinity difference between the sinking basin and the nonsinking basin is smaller when sinking occurs in the wide basin.

High salinity in the north of the sinking basin is always reinforced by a large cross-equatorial overturning cell,

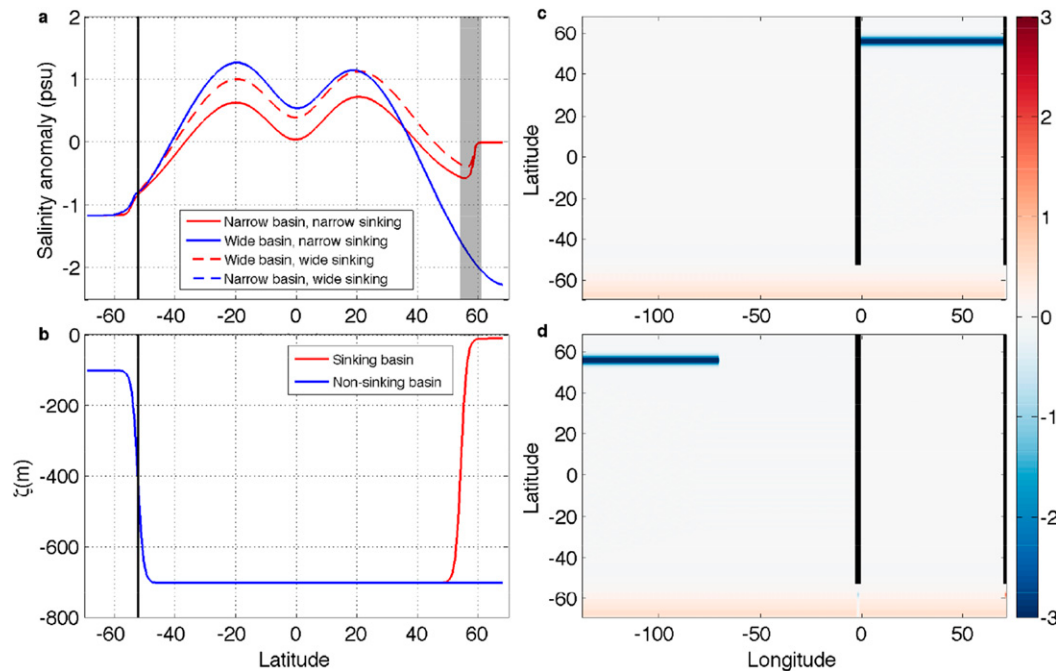


FIG. 15. (a) Zonally averaged salinity anomaly from the idealized 2D model using the velocity fields shown in Fig. 14, (b) the depth of the layer  $\zeta$  (m) and the diapycnal velocity  $\omega \times 10^6$  m s<sup>-1</sup> (c) for narrow sinking and (d) for wide sinking. In (a), the blue solid line and the blue dashed line are on top of each other.

which transports salt northward across the equator: this is the salt advection positive feedback (Stommel 1961). However, this feedback is less effective for wide sinking. In particular, for zonally uniform salinity flux, we show that the wide sinking state is unstable. This is because higher salinity (and therefore lower buoyancy) is found at the surface in the north of the narrow basin, and freshwater is more efficiently advected southward by the subpolar wind-driven gyre in the wide basin. The temperature advection negative feedback also plays a small role. When the width of the narrow basin is reduced further, keeping the width of the wide basin constant, the salinity difference between the basins increases, as does the preference for narrow sinking.

A 2D advection–diffusion model shows that the advection of salinity in the upper branch of the 3D overturning is well represented by the velocity vertically integrated above the isopycnal that divides the upper and lower branch of the MOC. The vertically integrated velocities show that there is a crucial difference in the sense of circulation on the western side of the SPG between the wide and narrow sinking basins. For narrow sinking, the western boundary current in the SPG is very weak, and for wide sinking it is strong and southward, advecting freshwater from the north, forming a halocline that is absent in the narrow sinking basin. This halocline is advected eastward by

the southern branch of the SPG, suppressing deep-water mass formation.

We rationalize the difference between narrow and wide sinking by invoking the linear superposition of the western boundary velocities associated with the wind-driven SPG and with the MOC. The latter is independent of the basin size, while the former is larger for a wide basin, and it prevails over the MOC in the wide sinking basin. This is consistent with Warren's (1983) suggestion that the small flow rate between the subtropical gyre and the SPG in the Pacific leads to lower salinities in the North Pacific when sinking is in the Atlantic and with the observations of Hátún et al. (2005) and Häkkinen and Rhines (2004) that salinity in the North Atlantic increases with decreasing SPG strength. We extend Warren's idea by showing that even when sinking is induced in the Pacific, the salt advection feedback is less effective there because of the stronger Sverdrup SPG circulation.

We further emphasize the interaction of the gyral velocities with the MOC by contrasting the effect of the two velocity components in isolation. Advection by gyres-only velocities or MOC-only velocities leads to no preference for narrow sinking.

Our arguments work well in the idealized context of our model, with simple coastlines, flat bottom, and

zonally uniform steady forcing. There is evidence that topographic steering alters the position of the intergyre boundary (Zhang and Vallis 2007), as does time dependence caused by well-resolved eddies, even in idealized geometries (Lévy et al. 2010). Thus, it is not clear how robust the narrow sinking preference is in more complex settings.

Models with realistic geometry and forcing find that the transport of the SPG in the North Atlantic is about 20 Sv (Bryan et al. 1995; Eden and Willebrand 2001), which is only slightly larger than the 18-Sv observational estimate of the transport of the MOC in the North Atlantic (Talley 2013). The strength of the Pacific SPG western boundary current in the CCSM4 model (Gent et al. 2011) is resolution dependent, but in CCSM4 T31 (a high-resolution run), the transport of the Pacific SPG is about 30 Sv, which would be sufficient to overwhelm the 18-Sv MOC transport. It is difficult to compare observations of the SPG transport between the Atlantic and Pacific because most long-term observations are limited to 2000-m depth and hence include the upper branch of the MOC. Deep-water formation largely occurs in marginal seas rather than in the open ocean, as it does in our model. Despite these caveats, our results indicate that the Atlantic's narrowness is a favorable asymmetry for sinking, which adds to the freshwater flux asymmetry.

**Acknowledgments.** CSJ and PC are supported by the National Science Foundation under Grants OCE-1258887 and OCE-1634128. Computational resources were provided by the XSEDE consortium, which is supported by National Science Foundation Grant ACI-1053575. CSJ thanks Ian Eisenman and Eric Chassignet for valuable conversations, and both CSJ and PC thank the two anonymous reviewers for their helpful comments on this work.

## APPENDIX A

### The 2D Advection–Diffusion Equation

To simplify the advection–diffusion equation, we integrate (7) vertically from the depth  $\zeta(\tilde{t}, \tilde{x}, \tilde{y}, \tilde{b} = b_m)$  to the surface, where  $b_m$  is a constant. This gives

$$\begin{aligned} & \int_{\zeta}^0 S_t dz + \int_{\zeta}^0 (uS)_x dz + \int_{\zeta}^0 (vS)_y dz - wS|_{\zeta} \\ &= \int_{\zeta}^0 \nabla \cdot (\mathbf{K} \nabla S) dz - FS_{\text{ref}} - \kappa_v S_z|_{\zeta}, \end{aligned} \quad (\text{A1})$$

where the Redi tensor is defined as

$$\mathbf{K} \equiv \kappa_{\text{GM}} \begin{pmatrix} 1 & 0 & -\frac{b_x}{b_z} \\ 0 & 1 & -\frac{b_y}{b_z} \\ -\frac{b_x}{b_z} & -\frac{b_y}{b_z} & \left| \frac{\nabla_h b}{b_z} \right|^2 \end{pmatrix}, \quad (\text{A2})$$

and  $\kappa_{\text{GM}}$  is the Gent–McWilliams diffusion coefficient. Substituting  $\mathbf{K}$  into (A1) and expanding the Redi matrix yields

$$\begin{aligned} & \int_{\zeta}^0 S_t dz + \int_{\zeta}^0 (uS)_x dz + \int_{\zeta}^0 (vS)_y dz - wS|_{\zeta} \\ &= \frac{\text{Redi}}{\text{terms}} - FS_{\text{ref}} - \kappa_v S_z|_{\zeta}, \end{aligned} \quad (\text{A3})$$

where

$$\begin{aligned} \text{Redi} &= \int_{\zeta}^0 \left[ \kappa_{\text{GM}} \left( S_x - \frac{b_x}{b_z} S_z \right) \right]_x + \left[ \kappa_{\text{GM}} \left( S_y - \frac{b_y}{b_z} S_z \right) \right]_y \\ &+ \left[ \kappa_{\text{GM}} \left( -\frac{b_x}{b_z} S_x - \frac{b_y}{b_z} S_y + \left| \frac{\nabla_h b}{b_z} \right|^2 S_z \right) \right]_z dz. \end{aligned} \quad (\text{A4})$$

A substantial simplification of (A3) and (A4) is obtained by moving from Eulerian coordinates  $(x, y, z, t)$  to buoyancy coordinates  $(\tilde{x}, \tilde{y}, \tilde{b}, \tilde{t})$ , using the rules (21) to (24) in WRY12. Because  $\zeta_x = \zeta_y = \zeta_t = 0$ , the horizontal derivatives can be moved outside the vertical integral giving

$$\begin{aligned} & \left( \int_{\zeta}^0 S dz \right)_t + \left( \int_{\zeta}^0 uS dz \right)_x + \left( \int_{\zeta}^0 vS dz \right)_y - wS|_{\zeta} \\ &= \frac{\text{Redi}}{\text{terms}} - FS_{\text{ref}} - \kappa_v S_z|_{\zeta}, \end{aligned} \quad (\text{A5})$$

where

$$\begin{aligned} \text{Redi} &= \left( \int_{\zeta}^0 \kappa_{\text{GM}} S_{\tilde{x}} dz \right)_x + \left( \int_{\zeta}^0 \kappa_{\text{GM}} S_{\tilde{y}} dz \right)_y \\ &+ \kappa_{\text{GM}} \left( \frac{b_x}{b_z} S_{\tilde{x}} + \frac{b_y}{b_z} S_{\tilde{y}} \right)|_{\zeta}. \end{aligned} \quad (\text{A6})$$

Notice that so far there are derivatives with respect to both buoyancy and Eulerian coordinates. Changing all derivatives from Eulerian coordinates  $(x, y, z, t)$  to buoyancy coordinates  $(\tilde{x}, \tilde{y}, \tilde{b}, \tilde{t})$  and using (28) in WRY12, we obtain

$$\begin{aligned} & \left( \int_{\zeta}^0 S dz \right)_{\bar{t}} + \left( \int_{\zeta}^0 u S dz \right)_{\bar{x}} + \left( \int_{\zeta}^0 v S dz \right)_{\bar{y}} \\ & + (\zeta_{\bar{t}} + u \zeta_{\bar{x}} + v \zeta_{\bar{y}} - w) S|_{\zeta} = \left( \int_{\zeta}^0 \kappa_{GM} S_{\bar{x}} dz \right)_{\bar{x}} \\ & + \left( \int_{\zeta}^0 \kappa_{GM} S_{\bar{y}} dz \right)_{\bar{y}} - FS_{ref} - \kappa_v S_z|_{\zeta}. \end{aligned} \quad (A7)$$

We separate velocity and salinity into a vertical average from  $\zeta$  to the surface, denoted by an overbar, and a departure from this average, denoted by prime, that is,  $u = \bar{u} + u'$ ,  $v = \bar{v} + v'$ , and  $S = \bar{S} + S'$ , and neglect quadratic terms in  $u'$ ,  $v'$ , or  $S'$ . Using (33) in WRY12, that is,

$$w = \zeta_{\bar{t}} + u \zeta_{\bar{x}} + v \zeta_{\bar{y}} + \frac{\varpi}{b_z}, \quad (A8)$$

where  $\varpi/b_z$  is the diapycnal term, we finally obtain

$$\begin{aligned} & (-\zeta \bar{S})_{\bar{t}} + (U \bar{S})_{\bar{x}} + (V \bar{S})_{\bar{y}} - \frac{\varpi}{b_z} S|_{\zeta} \\ & = -(\zeta \kappa_{GM} \bar{S}_{\bar{x}})_{\bar{x}} - (\zeta \kappa_{GM} \bar{S}_{\bar{y}})_{\bar{y}} - FS_{ref} - \kappa_v S_z|_{\zeta}. \end{aligned} \quad (A9)$$

## APPENDIX B

### Salinity Scaling for Advection by Gyres-Only Velocity

Here, we illustrate how the difference in salinity between the SPG and subtropical gyre scales with the external parameters, assuming that the gyre velocities are horizontally nondivergent. With no diapycnal velocity, (8) becomes

$$U_{gyre} \bar{S}_x + V_{gyre} \bar{S}_y \approx -FS_{ref} + \nabla \cdot (-\zeta \kappa_{GM} \nabla \bar{S}), \quad (B1)$$

where we have neglected time dependence and diapycnal and Redi diffusion. Integrating over the area  $A$ , enclosed by the outermost closed streamline of the SPG, we have

$$\int_A FS_{ref} da = - \oint_C \zeta \kappa_{GM} \nabla \bar{S} \cdot \mathbf{n} dl, \quad (B2)$$

where  $C$  is the arclength along the boundaries between gyres and  $\mathbf{n}$  is a unit vector perpendicular to that boundary. The solid boundaries have no diffusive flux, so the difference in salinity between the subtropical and subpolar gyre  $\Delta S$  is dominated by the diffusion at the intergyre boundary on the RHS of (B2). Thus,  $\Delta S$  scales as

$$\Delta S \sim \frac{FS_{ref} A \delta}{L_x \zeta \kappa_{GM}}, \quad (B3)$$

where  $\delta$  is the north-south thickness of the diffusive boundary layer. The value of  $\delta$  can be determined by the local advective-diffusive balance along the intergyre boundary:

$$U_{gyre} \bar{S}_x \approx -(\zeta \kappa_{GM} \bar{S}_y)_y, \quad (B4)$$

which gives the scaling  $\delta \sim \sqrt{\zeta \kappa_{GM} L_x / U_{gyre}}$ . Using Sverdrup balance and continuity to determine  $U_{gyre}$ , we finally get

$$\Delta S \sim FS_{ref} L_y \sqrt{\frac{\beta \rho}{\zeta \kappa_{GM} \tau_{yy}}}, \quad (B5)$$

where  $\beta \equiv d\ell/dy$  is the derivative of the Coriolis parameter,  $\rho$  is the mean density, and  $\tau$  is the wind stress at the intergyre boundary. Notice that the resulting  $\Delta S$  is independent of the basin width  $L_x$ .

## REFERENCES

- Allison, L. C., 2009: Spin-up and adjustment of the Antarctic Circumpolar Current and global pycnocline. Ph.D. thesis, University of Reading, 207 pp.
- Andrews, D. G., and M. E. McIntyre, 1978: Generalized Eliassen-Palm and Charney-Drazin theorems for waves on axisymmetric mean flows in compressible atmospheres. *J. Atmos. Sci.*, **35**, 175–185, [https://doi.org/10.1175/1520-0469\(1978\)035<175:GEPACD>2.0.CO;2](https://doi.org/10.1175/1520-0469(1978)035<175:GEPACD>2.0.CO;2).
- Broecker, W. S., 1991: The great ocean conveyor. *Oceanography*, **4**, 79–89, <https://doi.org/10.5670/oceanog.1991.07>.
- , T. H. Peng, J. Jouzel, and G. Russell, 1990: The magnitude of global fresh-water transports of importance to ocean circulation. *Climate Dyn.*, **4**, 73–79, <https://doi.org/10.1007/BF00208902>.
- Bryan, F. O., C. W. Böning, W. R. Holland, F. O. Bryan, and W. R. Holland, 1995: On the midlatitude circulation in a high-resolution model of the North Atlantic. *J. Phys. Oceanogr.*, **25**, 289–305, [https://doi.org/10.1175/1520-0485\(1995\)025<0289:OTMCIA>2.0.CO;2](https://doi.org/10.1175/1520-0485(1995)025<0289:OTMCIA>2.0.CO;2).
- Cessi, P., and C. S. Jones, 2017: Warm-route versus cold-route interbasin exchange in the meridional overturning circulation. *J. Phys. Oceanogr.*, **47**, 1981–1997, <https://doi.org/10.1175/JPO-D-16-0249.1>.
- Craig, P., D. Ferreira, and J. Methven, 2016: The contrast between Atlantic and Pacific surface water fluxes. *Tellus*, **69A**, 1330454, <https://doi.org/10.1080/16000870.2017.1330454>.
- Danabasoglu, G., and J. C. McWilliams, 1995: Sensitivity of the global ocean circulation to parameterizations of mesoscale tracer transports. *J. Climate*, **8**, 2967–2987, [https://doi.org/10.1175/1520-0442\(1995\)008<2967:SOTGOC>2.0.CO;2](https://doi.org/10.1175/1520-0442(1995)008<2967:SOTGOC>2.0.CO;2).
- Eden, C., and J. Willebrand, 2001: Mechanism of interannual to decadal variability of the North Atlantic circulation. *J. Climate*, **14**, 2266–2280, [https://doi.org/10.1175/1520-0442\(2001\)014<2266:MOITDV>2.0.CO;2](https://doi.org/10.1175/1520-0442(2001)014<2266:MOITDV>2.0.CO;2).
- Ferrari, R., S. M. Griffies, A. J. G. Nurser, and G. K. Vallis, 2010: A boundary-value problem for the parameterized mesoscale eddy transport. *Ocean Modell.*, **32**, 143–156, <https://doi.org/10.1016/j.ocemod.2010.01.004>.

- Ferreira, D., J. Marshall, and J.-M. Campin, 2010: Localization of deep water formation: Role of atmospheric moisture transport and geometrical constraints on ocean circulation. *J. Climate*, **23**, 1456–1476, <https://doi.org/10.1175/2009JCLI3197.1>.
- Geay, J. E., M. A. Cane, and N. Naik, 2003: Warren revisited: Atmospheric freshwater fluxes and “Why is no deep water formed in the North Pacific?” *J. Geophys. Res.*, **108**, 3178, <https://doi.org/10.1029/2001JC001058>.
- Gent, P. R., and J. C. McWilliams, 1990: Isopycnal mixing in ocean circulation models. *J. Phys. Oceanogr.*, **20**, 150–155, [https://doi.org/10.1175/1520-0485\(1990\)020<0150:IMIOCM>2.0.CO;2](https://doi.org/10.1175/1520-0485(1990)020<0150:IMIOCM>2.0.CO;2).
- , and Coauthors, 2011: The Community Climate System Model version 4. *J. Climate*, **24**, 4973–4991, <https://doi.org/10.1175/2011JCLI4083.1>.
- Gnanadesikan, A., 1999: A simple predictive model for the structure of the oceanic pycnocline. *Science*, **283**, 2077–2079, <https://doi.org/10.1126/science.283.5410.2077>.
- Gordon, A. L., J. R. E. Lutjeharms, and M. L. Gründlingh, 1987: Stratification and circulation at the Agulhas retroflection. *Deep-Sea Res.*, **34A**, 565–599, [https://doi.org/10.1016/098-0149\(87\)90006-9](https://doi.org/10.1016/098-0149(87)90006-9).
- Häkkinen, S., and P. B. Rhines, 2004: Decline of subpolar North Atlantic circulation during the 1990s. *Science*, **304**, 555–559, <https://doi.org/10.1126/science.1094917>.
- Hátún, H., A. B. Sandø, H. Drange, B. Hansen, and H. Valdimarsson, 2005: Influence of the Atlantic Subpolar Gyre on the thermo-haline circulation. *Science*, **309**, 1841–1844, <https://doi.org/10.1126/science.1114777>.
- Hewitt, C., R. Stouffer, A. Broccoli, J. Mitchell, and P. J. Valdes, 2003: The effect of ocean dynamics in a coupled GCM simulation of the Last Glacial Maximum. *Climate Dyn.*, **20**, 203–218, <https://doi.org/10.1007/s00382-002-0272-6>.
- Hughes, T. M. C., and A. J. Weaver, 1994: Multiple equilibria of an asymmetric two-basin ocean model. *J. Phys. Oceanogr.*, **24**, 619–637, [https://doi.org/10.1175/1520-0485\(1994\)024<0619:MEOAAT>2.0.CO;2](https://doi.org/10.1175/1520-0485(1994)024<0619:MEOAAT>2.0.CO;2).
- Huisman, S. E., H. A. Dijkstra, A. S. von der Heydt, W. P. M. de Ruijter, A. S. von der Heydt, and W. P. M. de Ruijter, 2012: Does net E–P set a preference for North Atlantic sinking? *J. Phys. Oceanogr.*, **42**, 1781–1792, <https://doi.org/10.1175/JPO-D-11-0200.1>.
- Jones, C. S., and P. Cessi, 2016: Interbasin transport of the meridional overturning circulation. *J. Phys. Oceanogr.*, **46**, 1157–1169, <https://doi.org/10.1175/JPO-D-15-0197.1>.
- Kamphuis, V., S. E. Huisman, and H. A. Dijkstra, 2011: The global ocean circulation on a retrograde rotating Earth. *Climate Past*, **7**, 487–499, <https://doi.org/10.5194/cp-7-487-2011>.
- Lévy, M., P. Klein, A.-M. Tréguier, D. Iovino, G. Madec, S. Masson, and K. Takahashi, 2010: Modifications of gyre circulation by sub-mesoscale physics. *Ocean Modell.*, **34**, 1–15, <https://doi.org/10.1016/j.ocemod.2010.04.001>.
- McCartney, M. S., and C. Mauritzen, 2001: On the origin of the warm inflow to the Nordic Seas. *Prog. Oceanogr.*, **51**, 125–214, [https://doi.org/10.1016/S0079-6611\(01\)00084-2](https://doi.org/10.1016/S0079-6611(01)00084-2).
- Nilsson, J., P. L. Langen, D. Ferreira, and J. Marshall, 2013: Ocean basin geometry and the salinification of the Atlantic Ocean. *J. Climate*, **26**, 6163–6184, <https://doi.org/10.1175/JCLI-D-12-00358.1>.
- Redi, M. H., 1982: Oceanic isopycnal mixing by coordinate rotation. *J. Phys. Oceanogr.*, **12**, 1154–1158, [https://doi.org/10.1175/1520-0485\(1982\)012<1154:OIMBCR>2.0.CO;2](https://doi.org/10.1175/1520-0485(1982)012<1154:OIMBCR>2.0.CO;2).
- Reid, J. L., 1961: On the temperature, salinity, and density differences between the Atlantic and Pacific Oceans in the upper kilometre. *Deep-Sea Res.*, **7**, 265–275, [https://doi.org/10.1016/0146-6313\(61\)90044-2](https://doi.org/10.1016/0146-6313(61)90044-2).
- , 1979: On the contribution of the Mediterranean Sea outflow to the Norwegian-Greenland Sea. *Deep-Sea Res.*, **26A**, 1199–1223, [https://doi.org/10.1016/0198-0149\(79\)90064-5](https://doi.org/10.1016/0198-0149(79)90064-5).
- Schmitt, R. W., P. S. Bogden, C. E. Dorman, R. W. Schmitt, P. S. Bogden, and C. E. Dorman, 1989: Evaporation minus precipitation and density fluxes for the North Atlantic. *J. Phys. Oceanogr.*, **19**, 1208–1221, [https://doi.org/10.1175/1520-0485\(1989\)019<1208:EMPADF>2.0.CO;2](https://doi.org/10.1175/1520-0485(1989)019<1208:EMPADF>2.0.CO;2).
- Schmittner, A., T. A. Silva, K. Fraedrich, E. Kirk, and F. Lunkeit, 2011: Effects of mountains and ice sheets on global ocean circulation. *J. Climate*, **24**, 2814–2828, <https://doi.org/10.1175/2010JCLI3982.1>.
- Seager, R., N. Naik, and G. A. Vecchi, 2010: Thermodynamic and dynamic mechanisms for large-scale changes in the hydrological cycle in response to global warming. *J. Climate*, **23**, 4651–4668, <https://doi.org/10.1175/2010JCLI3655.1>.
- , H. Liu, N. Henderson, I. Simpson, C. Kelley, T. Shaw, Y. Kushnir, and M. Ting, 2014: Causes of increasing aridification of the Mediterranean region in response to rising greenhouse gases. *J. Climate*, **27**, 4655–4676, <https://doi.org/10.1175/JCLI-D-13-00446.1>.
- Stocker, T. F., D. G. Wright, and W. S. Broecker, 1992: The influence of high-latitude surface forcing on the global thermohaline circulation. *Paleoceanography*, **7**, 529–541, <https://doi.org/10.1029/92PA01695>.
- Stommel, H., 1957: A survey of ocean current theory. *Deep-Sea Res.*, **4**, 149–184, [https://doi.org/10.1016/0146-6313\(56\)90048-X](https://doi.org/10.1016/0146-6313(56)90048-X).
- , 1961: Thermohaline convection with two stable regimes of flow. *Tellus*, **13**, 224–230, <https://doi.org/10.3402/tellusa.v13i2.9491>.
- Talley, L. D., 2008: Freshwater transport estimates and the global overturning circulation: Shallow, deep and throughflow components. *Prog. Oceanogr.*, **78**, 257–303, <https://doi.org/10.1016/j.pocean.2008.05.001>.
- , 2013: Closure of the global overturning circulation through the Indian, Pacific, and Southern Oceans: Schematics and transports. *Oceanography*, **26**, 80–97, <https://doi.org/10.5670/oceanog.2013.07>.
- Wang, X., P. H. Stone, and J. Marotzke, 1995: Poleward heat transport in a barotropic ocean model. *J. Phys. Oceanogr.*, **25**, 256–265, [https://doi.org/10.1175/1520-0485\(1995\)025<0256:PHTIAB>2.0.CO;2](https://doi.org/10.1175/1520-0485(1995)025<0256:PHTIAB>2.0.CO;2).
- Warren, B. A., 1981: Deep circulation of the World Ocean. *Evolution of Physical Oceanography*, B. A. Warren and C. Wunsch, Eds., MIT Press, 6–41.
- , 1983: Why is no deep water formed in the North Pacific? *J. Mar. Res.*, **41**, 327–347, <https://doi.org/10.1357/002224083788520207>.
- Weaver, A. J., C. M. Bitz, A. F. Fanning, and M. M. Holland, 1999: Thermohaline circulation: High-latitude phenomena and the difference between the Pacific and Atlantic. *Annu. Rev. Earth Planet. Sci.*, **27**, 231–285, <https://doi.org/10.1146/annurev.earth.27.1.231>.
- Wills, R. C., and T. Schneider, 2015: Stationary eddies and the zonal asymmetry of net precipitation and ocean freshwater forcing. *J. Climate*, **28**, 5115–5133, <https://doi.org/10.1175/JCLI-D-14-00573.1>.
- Young, W. R., 2012: An exact thickness-weighted average formulation of the Boussinesq equations. *J. Phys. Oceanogr.*, **42**, 692–707, <https://doi.org/10.1175/JPO-D-11-0102.1>.
- Zhang, R., and G. K. Vallis, 2007: The role of bottom vortex stretching on the path of the North Atlantic western boundary current and on the northern recirculation gyre. *J. Phys. Oceanogr.*, **37**, 2053–2080, <https://doi.org/10.1175/JPO3102.1>.